Diploma Thesis

Physics Department

University of Crete

Development of an imaging platform for in-vivo observations in mouse models using combined photoacoustic and optical microscopy

Supervisors: Dr. Giannis Zacharakis

Prof. Dimitris Charalampidis

Prof. Dimitris Papazoglou

Research Advisor: Dr. Giorgos Tserevelakis

Ntalopoulos Antonis

Heraklion, October 2018

Ευχαριστίες

Φτάνοντας στο τέλος των μεταπτυχιακών μου σπουδών, θα ήθελα να ευχαριστήσω μέσα από την καρδιά μου όλους εκείνους τους ανθρώπους που συνέδραμαν στην διεκπαιρέωση της παρούσας ερευνητικής εργασίας.

Κατ' αρχάς θα ήθελα να ευχαριστήσω θερμά τον ερευνητή, κ. Γιάννη Ζαχαράκη για την ανάθεση της εργασίας και την ευκαιρία που μου έδωσε να εμπλουτίσω παραπάνω τις γνώσεις μου τόσο σε πειραματικό επίπεδο όσο και από άποψη γνώσεων της φυσικής. Αισθάνομαι ειλικρινά ευγνώμων απέναντι στο πρόσωπό του, ειδικά για την εμπιστοσύνη που μου έδειξε από την πρώτη κίολας μέρα γνωριμίας μας.

Εν συνεχεία, θα ήθελα να ευχαριστήσω τον κ. Γιώργο Τσερεβελάκη, που ήταν υπεύθυνος για την εκπόνηση της μεταπτυχιακής μου εργασίας. Νιώθω τυχερός που κατάφερα να συνεργαστώ μαζί του. Είναι ένας άνθρωπος που αγαπάει εις το έπακρον αυτό που κάνει και του αρέσει να βοηθάει ανιδιοτελώς. Δεν θυμάμαι ούτε μία μέρα που να μην αποκτήσω μία επιπλέον γνώση από τον Γιώργο. Η βοήθειά του ήταν ανεκτίμητη και δεν θα τα κατάφερνα χωρίς αυτόν.

Αισθάνομαι βαθύτατα όμως την ανάγκη να ευχαριστήσω τους ανθρώπους που στάθηκαν δίπλα μου δίνοντάς μου κουράγιο να συνεχίσω. Υπήρξαν στιγμές όπου η απογοήτευση ηταν μεγάλη, οι αρνητικές σκέψεις πλημμύριζαν το μυαλό μου και το άγχος για την επίτευξη οποιουδήποτε στόχου με είχε καταβάλει. Μέσα σε όλους αυτούς είναι η αδερφή μου, η μητέρα μου, οι συγγενείς μου και οι φίλοι μου. Από τους φίλους μου θέλω να ξεχωρίσω τον Μανώλη Διακαναστάση και την συμφοιτήτρια Μαίρη Κεφαλογιάννη που αποτελούσαν για εμένα πηγή αισιοδοξίας. Τέλος θα ήθελα να ευχαριστήσω τους ανθρώπους που πίστεψαν σε εμένα αλλά και αυτούς που δεν πίστεψαν, διότι με έκαναν να πιστέψω εγω παραπάνω στον ευατό μου και να ξεπεράσω κατά πολύ τα όρια και τις αντοχές μου!

Table of Contents

Abstract

Photoacoustic microscopy (PAM) is a novel in vivo imaging modality whose contrast arises from the detection of acoustic waves generated through the photoacoustic (PA) arises from the detection of acoustic waves generated through the photoacoustic (PA) effect. According to the PA effect, light is absorbed by molecules and converted into heat; this causes a local thermoelastic expansion of the medium leading to the generation of an acoustic wave which is subsequently detected using an ultrasonic transducer.

In this work we have developed an imaging platform for label-free, in-vivo observations in mouse models, through the integration of PAM and confocal fluorescence microscopy (CFM) into a single instrument in order to provide complementary contrast modes. More specifically, PAM could image ear vasculature due to the high absorption of visible radiation by hemoglobin, whereas CFM recorded the intrinsic autofluorescence of skin tissue originating predominantly from elastin and collagen. For these in-vivo measurements we have used laboratory mice (BALB/c) which were anaesthetized using a mixture of isoflurane with oxygen supply. Mice were subsequently placed on a custom-made platform dedicated for the imaging of the ear region, which is beneficial for imaging due to its small thickness.

The information obtained by the recorded co-registered images could be used for the study of several pathological conditions such as cancer and metabolic disorders, drug delivery processes etc. establishing thus a powerful hybrid imaging protocol applied in fundamental biomedical research.

1. Introduction

What is the main reason for humans to be excited about life? It is the curiosity about researching, learning and creation! With a quick glance at ancient years, we can deduce that humans are deeply curious beings. They were observing the world, investigating and trying to explain the physical effects. About centuries ago, pioneer scientists could start to explain macroscopic observations such as the motion of planets and stars, interaction of light and matter, etc. Over the years, as humans' perception was enhanced, medicine and biology emerged as a result of a deeper understanding on how biomolecules interact at microscopic and macroscopic spatial scales.

The vast evolution of research set high goals for scientists. In order to uncover the microscopic biological world, several imaging techniques have been developed. Historically speaking the first imaging technique was the light microscope which consists a powerful tool for studying tissue components, molecules and organs [1].

However, the conventional microscope is inefficient for specific in depth tissue imaging of more than a few hundred of micrometers due to light scattering [2]. For decades, engineers were trying to surmount this scientific gap till the laser microscopy techniques came into view.

Laser microscopy is an implementation of optical microscopy that uses monochromatic laser sources for the illumination of the sample under investigation. There are plenty of laser microscopy techniques which can be classified in categories depending on their spatial resolution [3]. Among them, we will extensively analyze the photoacoustic microscopy (PAM) modality. PAM is a technique that takes advantage of the photoacoustic effect and will constitutes the major topic of the current thesis.

1.1 Photoacoustic effect

The discovery of the photoacoustic or optoacoustic effect dates back to 1880, when Alexander Graham Bell was experimenting with long-distance sound transmission. Through his invention, called "the photophone" (*Figure 1.1.1)*, he transmitted vocal signals by reflecting sun-light from a moving mirror to a selenium solar cell receiver. As a byproduct of this investigation, he observed that sound waves were produced directly from a solid sample when exposed to beam of sunlight that was rapidly interrupted with a rotating slotted wheel. He noticed that the resulting acoustic signal was dependent on the type of the material and correctly reasoned that the effect was caused by the absorbed light energy, which subsequently heats the sample [4].

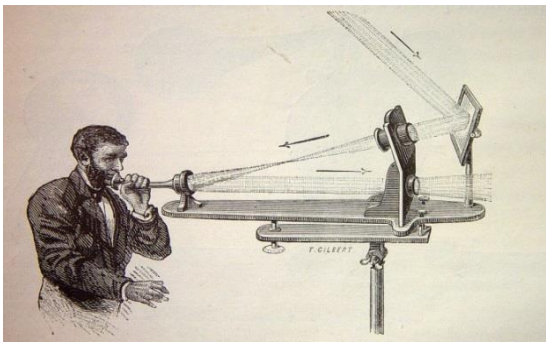

Figure 1.1.1: Bell's Photophone – The World's first cell phone.

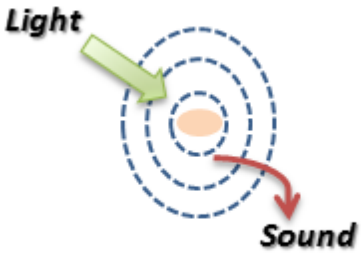

Figure 1.1.2: Photoacoustic effect.

The principle of the photoacoustic effect (*Figure 1.1.2)* is very simple shining a material with light produces acoustic waves. More specifically, the incident electromagnetic radiation in a material sample, is absorbed by molecules and their energy is partially converted into heat. The heat subsequently induces an initial pressure rise, which propagates as an acoustic wave [5]. To obtain this effect the light intensity must vary periodically [6].

1.2 Photoacoustic imaging

The photoacoustic imaging technique is based on the photoacoustic effect and is schematically illustrated in *Figure 1.2.1*. Typically, the sample is illuminated by a pulsed laser using short nanosecond pulses in the visible or near-infrared spectral range. The generated broadband acoustic waves are detected by an ultrasound transducer. In order to avoid the strong attenuation of the acoustic waves, a coupling medium (gel or water) is requires in the space between the sample and the transducer.

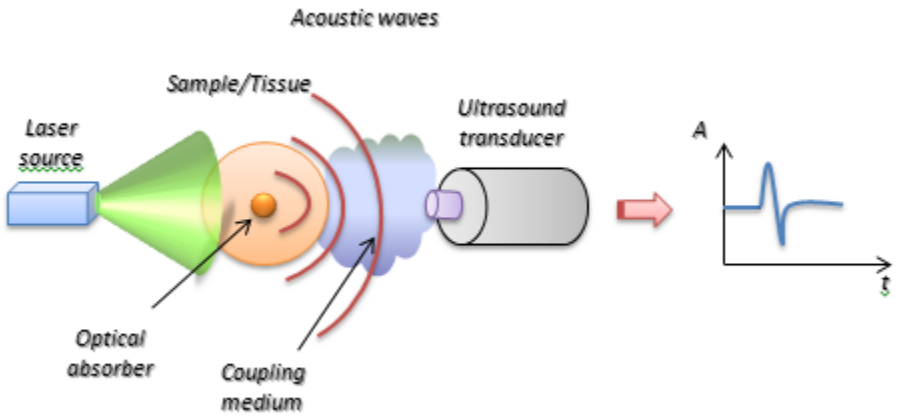

Figure 1.2.1: Basic principle of the photoacoustic effect.

Photoacoustic imaging can be divided into two major categories: PA Tomography (PAT) and PA microscopy (PAM); and its variants [7]. PAT is the most general and least restrictive imaging approach that shows great results for biological research and clinical practice.

In PAT, full field illumination is applied on the tissue surface; and acoustic waves can be recorded by unfocused transducers. The time-varying detected ultrasound signals can be spatially resolved and back-projected to form a three-dimensional image with the aid of a reconstruction algorithm [8]. Additionally, high imaging depths can be obtained (~5 cm) at resolutions in the order of hundreds of micrometers.

By contrast, in PAM a laser beam is focused (weakly or strongly) on the region under investigation. The detection of PA signals is achieved with spherical focused detectors. The image is obtained by raster scanning and formed directly from the set of acquired A-lines, without the aid of a reconstruction algorithm as in PAT. In comparison with PAT, PA microscopy gives shallower imaging depths (up to 3mm) at high resolutions [8]. According to the light and acoustic focusing, PAM can be further classified into optical resolution (OR-PAM) and acoustic resolution (AR-PAM). If the optical focus is much tighter than acoustic focus then OR-PAM dominates. Otherwise, AR-PAM takes precedence [9], [10].

A further distinction between PAT and AR-PAM lies in the complexity and cost of implementation. The laser power requirements for AR-PAM are more modest than those of PAT. In PAT, the entire three-dimensional FOV (field of view) must be irradiated whereas in AR-PAM only the region that coincides with the received beam profile of the transducer is required to be illuminated for each scan position. By confining the internal light distribution to this region by weak focusing, a laser pulse energy that is an order of magnitude lower than that required for PAT can be used. This allows a greater variety of laser sources to be used and a tunable output. AR-PAM can also be straightforwardly and inexpensively implemented as a laboratory-based research tool using a single mechanically scanned receiver.

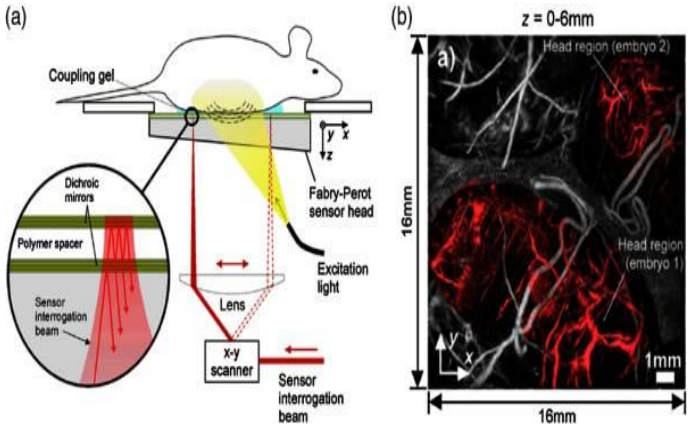

Figure 1.2.2: Fabry–Perot interferometer (FBI) based PACT system. *(a) Schematic and (b) a representative image of a FBI based PACT system. The red parts in (b) indicate the location of embryos [10].*

1.3 Hybrid photoacoustic microscopy

With the term "hybrid" we imply the combining of PAM with any other imaging technique. Recently developed optical-resolution photoacoustic microscopy (OR-PAM), which is based on the detection of optical absorption contrast, is complementary to other optical microscopy modalities such as optical confocal microscopy, optical coherence tomography, and multi-photon microscopy [11]. A hybrid optical–mechanical scanning configuration increases the imaging speed of OR-PAM significantly, enabling many demanding biomedical applications.

Figure 1.3.1 represents the hybrid imaging of rabbit eye's anterior segment. In this work they have been combined both PAM and CFM. It is demonstrated that the signals provided by each of the integrated modalities are spatially complementary and have the potential to offer high contrast anatomical information regarding the pars plana and pars plicata ciliary body portions, the iris, as well as, the attached zonule fiber strands [12].

Also, in *Figure 1.3.2* it is represented the hybrid imaging of the 6th and 7th groups in a USAF-1951 [13]. Combining light microscopy and PA image they manage to decode the numbers of the paper.

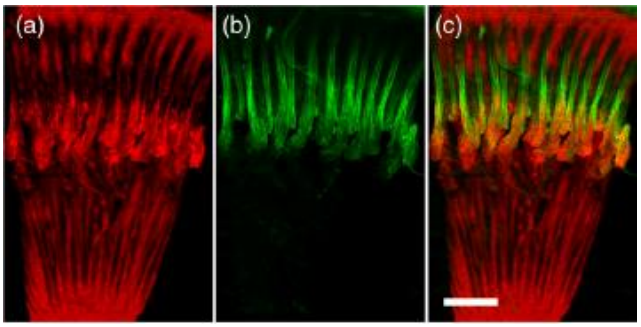

Figure 1.3.1: **Hybrid imaging of rabbit eye's anterior segment**. (a) PA image of ciliary body and iris. (b) Glutaraldehyde-induced AF image revealing the zonular fibrils. (c) Merged bimodal reconstruction. Scale bar is equal to 1 mm. [12]

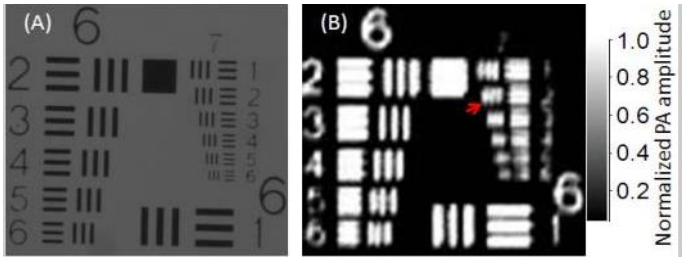

Figure 1.3.2: **Hybrid imaging of the 6th and 7th groups in a USAF-1951**.
(A) Light microscopy image and (B) maximum amplitude projection PA image of the 6th and 7th groups in a USAF-1951 resolution target acquired by the hybrid-scanning optical-resolution photoacoustic microscopy system. [13]

2. Theory

2.1 Photoacoustic microscopy (PAM)

Photoacoustic microscopy is a hybrid in vivo imaging technique, in the sense that both optics and acoustics are involved, which detects generated ultrasonic signals via photoacoustic effect. Using irradiation with nanosecond pulsed laser beam, tissues undergo a rapid thermoelastic expansion, resulting in the release of a wideband acoustic wave that can be detected using a high-frequency ultrasound transducer.

Since ultrasonic scattering in tissue is weaker than optical scattering by up to three orders of magnitude, photoacoustic microscopy is capable of achieving high-resolution images at greater depths than conventional optical microscopy methods [9].

In general, spatial resolution is essentially is the ability of an imaging system to distinguish between two points at a particular depth in a sample can be divided into lateral and axial resolution.

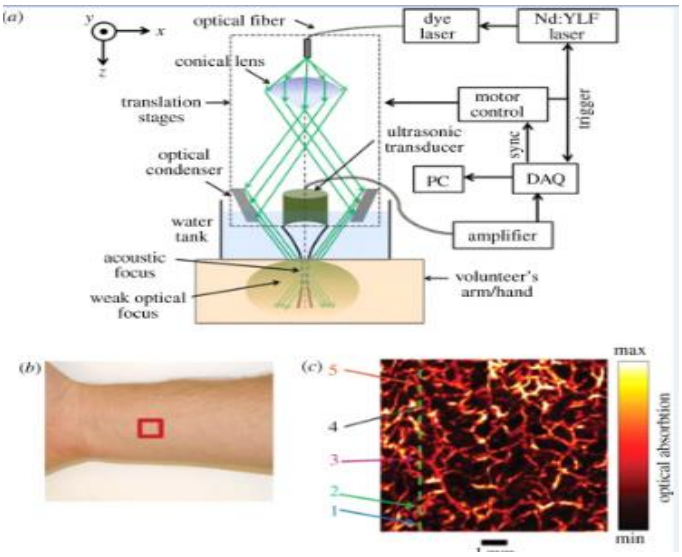

Figure 2.1.1: Acoustic resolution photoacoustic microscopy (AR-PAM) system used for imaging the skin vasculature. *(a) Schematic of system, (b) region of forearm scanned, (c) lateral x-y Maximum Intensity Projection image (Field Of View 8x8mm^2) [14].*

i) Lateral resolution

The lateral resolution $R_{L,OR}$ of OR-PAM is determined mainly by the numerical aperture of the objective lens (NA_0), which focuses the light to the sample and by the optical excitation wavelength (λ_0) :

$$R_{L,OR} = 0.51\frac{\lambda_0}{NA_0} \qquad (1.1)$$

The numerical aperture (NA_0) of an optical system is a dimensionless number that characterizes the range of angles over which the system can accept or emit light [15]. Assuming a thin lens with width D and focal length f, the numerical aperture is defined by,

$$NA_0 = n\,sin\theta \qquad (1.2)$$

, where n is the index of refraction of the medium in which the lens is working (1.00 for air, 1.33 for pure water, and typically 1.52 for immersion oil) [16].

$$NA_0 = nsin\theta \Rightarrow$$

$$NA_0 = nsin\left[\arctan\left(\frac{D}{2f}\right)\right] \Rightarrow$$

$$\boxed{NA_0 \cong \frac{nD}{2f}} \qquad (1.3)$$

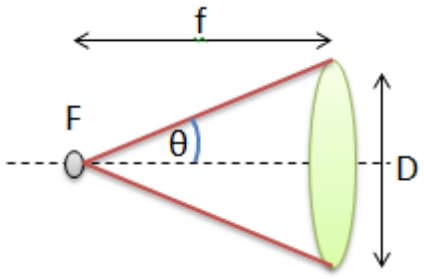

Figure 2.1.2: Numerical aperture of a thin lens.

The lateral resolution of OR-PAM can be scaled down by either increasing the objective NA_0 or using a shorter excitation wavelength, with the maximum imaging depth scaled accordingly.

In the same way, the lateral resolution of AR-PAM is given by,

$$R_{L,AR} = 0.71\frac{\lambda_A}{NA_A} = 0.71\frac{u_A}{NA_A \cdot f_A} \tag{1.4}$$

where NA_A is the numerical aperture of ultrasonic transducer, u_A is the speed of sound in the medium, and λ_A and f_A are the central wavelength and frequency of the photoacoustic signal respectively. The constant 0.71 results from the full width at half maximum of the acoustic focal spot in terms of acoustic amplitude [17].

ii) Axial resolution

For axial resolution, two techniques follow the same formula,

$$R_{A,OR/AR} = 0.88\frac{u_A}{\Delta f_A} \tag{1.5}$$

which is based on the assumption that the generated photoacoustic signal follows a Gaussian frequency profile [18]. The factor Δf_A corresponds to the bandwidth of the ultrasonic transducer. Usually, the bandwidth of an ultrasound sensor is proportional to its central frequency f_A.

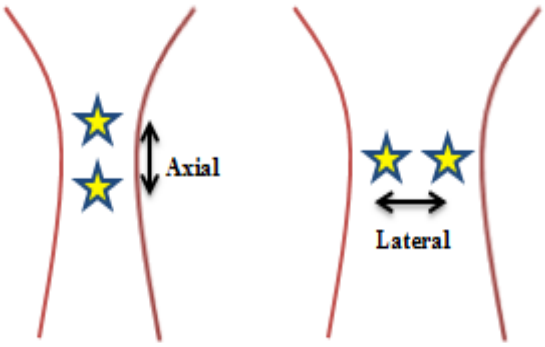

Figure 2.1.3: Axial & Lateral resolution.

2.1.1 Limiting factors in PAM

Like all imaging techniques, photoacoustic modality has its own boundaries and limitations. There are several factors that confine the capabilities of this imaging method such as imaging depth, signal to noise ratio and detection sensitivity.

Imaging Depth

It is known that strong scattering of visible light in tissue sets barriers on the imaging depth [2] of OR-PAM, which is limited to ~1 mm in tissue [16]. On the other hand, in AR-PAM technique, the imaging depth is primarily limited by the frequency dependent ultrasonic attenuation, but also by the optical excitation wavelength [18]. According to the way that light is scattered at different depths in tissue, three regimes can be defined.

The ballistic regime, in which there is no scattering event along a straight line or photons collided only one time and can be focused again to the spot. The range of this regime is determined by the mean free path (MFP). The MFP describes the average distance that a photon travels between two collisions. Since the absorption in tissues is much weaker than scattering, the MFP can be defined as [2],

$$MFP \cong 1/\mu_s \tag{1.6}$$

The MFP is of the order of 100 μm in tissue, although it varies with tissue type; it is shorter in highly scattering tissues such as brain and longer in low-scattering tissues such as naturally semitransparent organisms [2].

However, other methods such as confocal and multiphoton microscopy have been developed to image specimens thicker than 10–20 μm [2]. The penetration limit of these advanced methods is governed by a second physical parameter, the transport mean free path (TMFP) [2].

TMFP is a parameter that gives us information for the mean propagation distance before the photons change their direction. Moreover is defined as,

$$MFP = TMFP\,(1 - g) \tag{1.7}$$

where g is the anisotropy function defining the degree of forward scattering [2]. In tissue, typical values of g is 0.8-0.99 [2]. After this regime, the diffusion is very strong and light propagation occurs randomly.

Noise in photoacoustic imaging

Noise puts a brake on PAM detection of single molecules. The interacting medium and the ultrasonic detector are mainly responsible for this noise. The medium exhibits thermal acoustic noise that fundamentally limits the detection of any photoacoustic signal [20]. The distribution of noise is detected by the ultrasonic transducer and is given by,

$$N_a(f) = n_d(f)k_BT \tag{1.8}$$

where $n_d(f)$ is the transducer efficiency at frequency f, defined as the fraction of acoustic power converted to electrical power; k_B is the Boltzmann constant and T is the absolute temperature of the medium in Kelvin [20].
Moreover, an acoustic detector generates thermal noise due to its internal impedance. Assuming a piezoelectric transducer with a resistance matched to an amplifier with load resistance R, the power spectral density of noise is given by,

$$N_d(f) = k_BT \tag{1.9}$$

The amplifier also introduces additional electronic noise. To describe that kind of noise, there is a factor F_n, which denotes the noise factor of the amplifier and has a typical value of 2 over its bandwidth [20]. Finally, the electronic noise generated by the amplifier is giver by,

$$N_{am}(f) = N_d(f)(F_n - 1) \tag{1.10}$$

Detection sensitivity

The detection sensitivity is strongly related to the minimum quantity of absorber that is needed for detection. It is affected by the incident laser fluence, imaging depth, optical wavelength and the efficiency of the ultrasonic transducer [18]. In general, the greater the imaging depth is, the weaker signal sensitivity is. Thus, more quantity of absorber (contrast agent) is necessary. Consequently, the detection sensitivity is inversely proportional to imaging depth.

In biomedical imaging, two parameters can be used to quantify the detection sensitivity: noise-equivalent concentration (NEC) or the noise-equivalent number of molecules per resolution voxel (NEN). The latter is the aftermath of the former, while the resolution voxel volume associated with the noise from a voxel [18]. These parameters expressed in $nmol$ or mmol. Last but not least, the detection sensitivity can be enhanced by using exogenous contrast agents such as organic dyes with greater absorption cross sections.

2.1.2 Contrast agents for PAM

Photoacoustic microscopy can potentially image all molecules, vessels, cells, etc. [18]. Also, the PAM contrast can be obtained through endogenous or exogenous absorbers.

The endogenous contrast agents have indisputably more advantages. First and foremost, they are nontoxic; so they do not contaminate the tissue's microenvironment. Moreover, they are usually galore in tissues, do not require further cost and do not require time for regulation [21]. As shown below, endogenous absorbers can be classified into two groups according to their primary absorbing wavelengths.

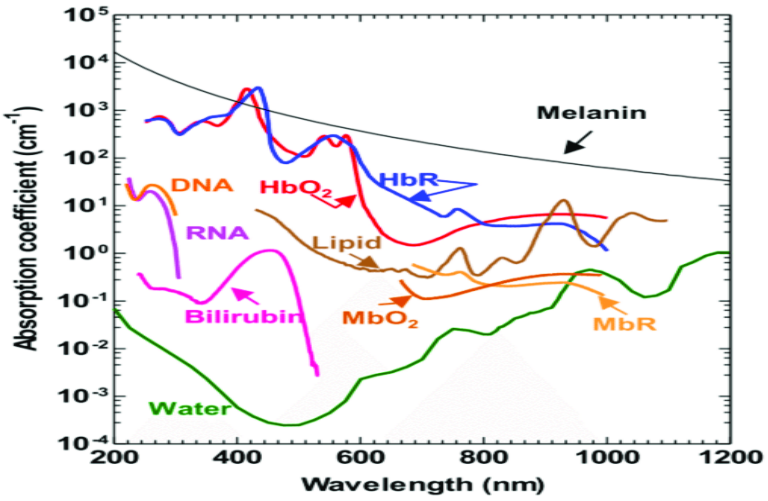

Figure 2.1.2.1: Absorption spectra of major endogenous contrast agents in biological tissue

In the ultraviolet (180nm to 400nm) and visible regions (400nm to 700nm) the dominant absorbers are DNA/RNA, cytochrome c, myoglobin, hemoglobin and melanin. Besides them, it is noticeable that DNA and RNA absorb mainly in the UV region. Since cancer cells tend to spontaneously accumulation and have unusual morphology, UV-PAM can be used for cancer diagnosis and intraoperative cancer cell detection [22]. Nevertheless, the cells can be damaged by overexposure to UV light and DNA might be distorted too.

The hemoglobin is the most abundant protein in blood and the major oxygen carrier. A series of biological applications such as hemoglobin concentration, oxygen saturation and blood flow speed has been performed by PAM technique [20]. Also, melanin is an ideal contrast agent due to high optical absorption in the UV-VIS region. PAM has been successfully applied for melanoma detection, which is the foremost killer among skin cancers [21].

In the near-infrared region (700nm-1400nm), lipid, water and glucose are the major absorbers. A persistently high blood glucose level is referred to as hyperglycemia; low levels are referred to as hypoglycemia. Diabetes mellitus is characterized by persistent hyperglycemia from any of several causes, and is the most prominent disease related to failure of blood sugar regulation [23]. Photoacoustic sensing has been applied both in vitro and in humans in order to measure the index of blood glucose with very good precision.

Exogenous contrast agents such as organic dyes, nanoparticles, fluorescent proteins have been used in PAM allowing chemical, molecular and genetic imaging. One advantage over the endogenous absorbers is the maximum detection sensitivity. Due to their properties, optical and chemical, they can be used to enhance the detection sensitivity. Furthermore, they can be engineered to aim at a specific cell receptor. Methylene blue, which is a thiazine dye, has been used for sentinel lymph node imaging for cancer biopsy [24].

2.2 Photoacoustic signal generation

In order to obtain a fundamental equation that can describe the photoacoustic signals generation, let's begin with the follow assumption. A laser pulse is incident on a certain tissue region leading to a fractional volume expansion, which can be defined as

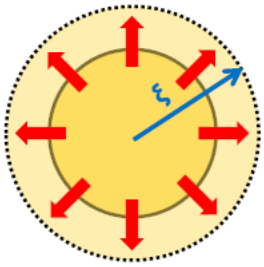

Figure 2.2.1: Volume expansion.

$$\vec{\nabla} \cdot \vec{\xi}(\vec{r}, t) = -\kappa P(\vec{r}, t) + \beta T(\vec{r}, t) \tag{2.1}$$

where $\vec{\xi}$ denotes the medium displacement from the equilibrium state, κ is the isothermal compressibility, β is the isothermal expansion and $P(\vec{r}, t), T(\vec{r}, t)$ are the spatiotemporal functions for pressure and temperature respectively.

Thermodynamically, κ and β are defined as

$$\kappa = -\frac{1}{V}\left(\frac{\partial V}{\partial P}\right)_T$$

Corresponds to the fractional change of volume while changing the pressure at a constant temperature.

$$\beta = \frac{1}{V}\left(\frac{\vartheta V}{\vartheta T}\right)_P$$

Expressing the fractional change of volume while changing temperature at a constant pressure.

The equation (2.1) indicates that the volume density of the outward flux of the vector $\vec{\xi}(\vec{r},t)$ from an infinitesimal volume around a given point is equal to the sum of two factors:

The first one is related to the exerted pressure, whereas the second one is a function of the object's temperature. Positive pressures tend to "shrink" the object – this explains the minus sign of the first term. On the other hand, the second factor expresses a linear relation of the volume expansion with the temperature -the more the object is heated the more it will expand.

If the pulse is extremely short, the fractional volume change is negligible and the initial pressure rise $p_0(\vec{r})$ directly after the excitation can be written as

$$p_0(\vec{r}) = \frac{\beta T(\vec{r})}{\kappa} = \Gamma \eta_{th} \mu_\alpha F \qquad (2.2)$$

where Γ is the Grueneisen parameter defined as $\Gamma = \frac{\beta u_s^2}{C_P}$, with u_s represents the speed sound in the medium and C_P denotes the specific heat capacity at a constant pressure, η_{th} is the percentage of absorbed energy that is covered to heat, μ_α is the optical absorption coefficient (cm^{-1}), and F is the optical fluence (J/cm^2).

The equation (2.2) is valid only if two conditions are fulfilled. The first one is that the laser pulse must be shorter that the thermal relaxation time

$$\tau_{th} = \frac{d_h^2}{a_{th}^2} \qquad (2.3)$$

where d_h represents the characteristic dimension of the heated volume and a_{th} denotes the thermal diffusivity (m^2/s). Second, the laser pulse must be shorter than the stress relaxation time

$$\tau_{st} = \frac{d_h}{u_s} \qquad (2.4)$$

2.3 Wave equation and forward solution

The generation of an initial pressure rise induces a bipolar (positive and negative values) acoustic wave that propagates through the medium and can be detected by an ultrasound transducer. Under the condition of thermal confinement (i.e heat conduction is negligible during the laser pulse), the wave equation for the pressure $p(\vec{r},t)$ is given by,

$$\boxed{\left(\nabla^2 - \frac{1}{u_s^2}\frac{\vartheta^2}{\vartheta t^2}\right)p(\vec{r},t) = -\frac{\beta}{C_P}\frac{\vartheta H(\vec{r},t)}{\vartheta t}} \tag{2.5}$$

The left-hand side of the equation describes the pressure wave propagation, and the right-hand side represents the source term with $H(\vec{r},t)$ denotes the heating function (W/cm^3). Therefore, time-invariant heating does not produce a pressure wave; only time-variant heating does!

Additionally, $H(\vec{r},t)$ can be further decomposed as the product of the respective spatial and temporal parts in the following form:

$$H(\vec{r},t) = H_S(\vec{r})H_T(t) \tag{2.6}$$

, whereas $H_S(\vec{r})$ represents the local deposited energy density in J/m^3 and $H_T(t)$ is the temporal excitation profile *(e.g. a Gaussian pulse)*.

Hence, the equation (2.5) is reduced to,

$$\left(\nabla^2 - \frac{1}{u_s^2}\frac{\vartheta^2}{\vartheta t^2}\right)P(\vec{r},t) = -\frac{\beta H_S(\vec{r})}{C_P}\frac{\vartheta H_T(t)}{\vartheta t} \tag{2.7}$$

- In case that $H_T(t) = \delta(t)$ *(i.e. impulse temporal excitation)*, we finally have

$$\left(\nabla^2 - \frac{1}{u_s^2}\frac{\vartheta^2}{\vartheta t^2}\right)P(\vec{r},t) = -\frac{\beta H_S(\vec{r})}{C_P}\frac{\vartheta \delta(t)}{\vartheta t} \tag{2.8}$$

The forward solution to the wave equation (2.5) is based on the Green's function approach, which is the response to a spatial and temporal delta source of the differential equation

$$\left(\frac{1}{u_s^2}\frac{\vartheta^2}{\vartheta t^2} - \nabla^2\right) G(\vec{r}, t) = \delta^3(\vec{r})\delta(t) \tag{2.9}$$

The Green's function in this equation describes the response of a point acoustic source following the excitation with a step heating function or a ramp temperature rise, since the source term is proportional to the first time derivative of the heating function or the second time derivative of the temperature in general.

With the Green function the solution of (2.5) can be expressed as

$$p(\vec{r}, t) = -\iiint_V \int_t G(\vec{r} - \vec{r}', t - t')\frac{\beta}{C_P}\frac{\vartheta H(\overrightarrow{r'}, t')}{\vartheta t'} d^3r'dt' \tag{2.10}$$

The free-space Green function has the following form

$$G(\vec{r} - \vec{r}', t - t) = -\frac{\delta\left(t - t' - \frac{|\vec{r} - \vec{r}'|}{u_s}\right)}{4\pi|\vec{r} - \vec{r}'|} \tag{2.11}$$

By inserting this expression into (2.10), the forward solution can be written as

$$\boxed{p(\vec{r}, t) = \iiint_V \int_t \frac{\delta\left(t - t' - \frac{|\vec{r} - \vec{r}'|}{u_s}\right)}{4\pi|\vec{r} - \vec{r}'|}\frac{\beta}{C_P}\frac{\vartheta H(\overrightarrow{r'}, t')}{\vartheta t'} d^3r'dt} \tag{2.12}$$

2.4 Background on fluorescence microscopy

Fluorescence microscopy is an invaluable tool in biology, since it constitutes a unique technique that is used to image features of small specimens with exceptional contrast and high specificity [25]. It is also used to visualize 3D biological samples at small spatial scales.

On the previous section it became clear that the photoacoustic effect occurs only when the light intensity varies, so a pulsed laser is needed. In most cases, a typrical ns pulsed laser emits at a specific wavelength, with limited wavelength tenability capabilities at reasonable cost. On the other hand, it is well known that endogenous absorbers in biological tissues exhibit autofluorescence (AF) properties, following their excitation with primary absorbing wavelengths [18]. For this reason, one more technique was combined with PAM in that thesis. This technique was the confocal fluorescence microscopy (CFM) and was mainly employed to offer a complementary contrast source.

2.4.1 Single excitation fluorescence

Fluorescence is defined as the spontaneous emission of light (optical frequencies) by a substance that has been excited electromagnetically (light absorption) or mechanically (friction); it is a form of luminescence. In most cases the emitted photons have a longer wavelength and therefore lower energy, than the incident absorbed photons. Generation of luminescence through excitation of a molecule by ultraviolet or visible light photons is a phenomenon termed photoluminescence, which is formally divided into two categories, fluorescence and phosphorescence, depending upon the electronic configuration of the excited state and the emission pathway. In order to have a comprehensive approach, we will begin with the principles of a simple spin system.

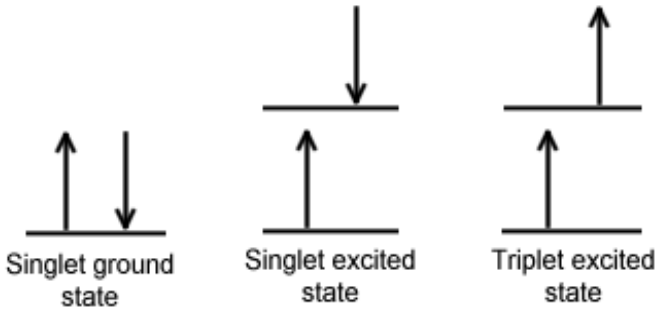

Figure 2.4.1.1: Singlet and triplet state of a spin system.

Based on the quantum mechanics, spin is a dimensionless number which essentially denotes the identity of its particle. Electrons for example have spin ½. The singlet and triplet states of a molecule are related to the spin states of its electrons. According to the *Pauli principle*, two electrons with the same spin cannot be together in the same orbital. The case where two electrons have opposite spin in the same orbital, is called *singlet state*, and the total spin is zero ($S = 0$). For an excited singlet state, one electron is found in a higher energy level orbital; however the two electrons constitute a pair with opposite spins. On the contrary, if one electron has been excited and maintain the same spin with the non-excited electron, the case is called *triplet state*, and the net spin is one ($S = 1$).

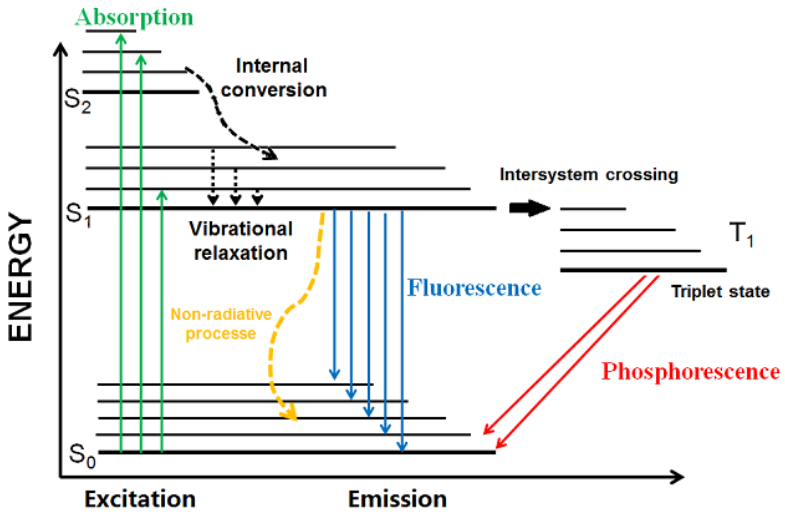

Figure 2.4.1.2: Schematic representation of single photon absorption, fluorescence and phosphorescence processes (Jablonski diagram).

The thick lines shown in *Figure 2.4.1.2* (S_1 *and* S_0) represent the excited and the ground singlet state of the molecule, while the parallel thinner lines represent its vibrational levels respectively. The energy difference between two electron states is comparable to the energy of a photon in the ultraviolet or visible region of the electromagnetic spectrum, while the energy difference between two sequential vibrational levels corresponds to the energy of an infrared photon (in the order of 0.1 *eV*). *Fluorescence* is most often observed between the first excited electron state and the ground state for any particular molecule because at higher energies it is more likely that energy will be dissipated through internal conversion and vibrational relaxation [26].

An another important procedure, called *phosphorescence*, occurs with the electronic transition from the first excited triplet state (T_1) to the ground singlet state (S_0). Phosphorescence is much slower process than fluorescence, since a triplet to singlet transition is much less probable [27].

Once an electron is excited, there are several ways that energy may be dissipated. The first is through *vibrational relaxation*, a non-radiative process. Vibrational relaxation is where the energy deposited by the photon into the electron is given away to other vibrational modes as kinetic energy. This process is also very fast, between 10^{-14} and 10^{-11} seconds. Since this is a very fast transition, it is extremely likely to occur immediately following absorbance [26], [27].

However, if vibrational energy levels overlap electronic energy levels, the excited electron can transition from a vibration level in one electronic state to another vibration level in a lower electronic state. This process is called *internal conversion*. Due to a lack of vibrational and electronic energy state overlap and a large energy difference between the ground state and first excited state, internal conversion is very slow for an electron to return to the ground state [26], [27].

The dissipation of the energy leads to a shift of the fluorescence into larger wavelengths (red shift) compared with the excitation irradiation is called *Stokes shift*.

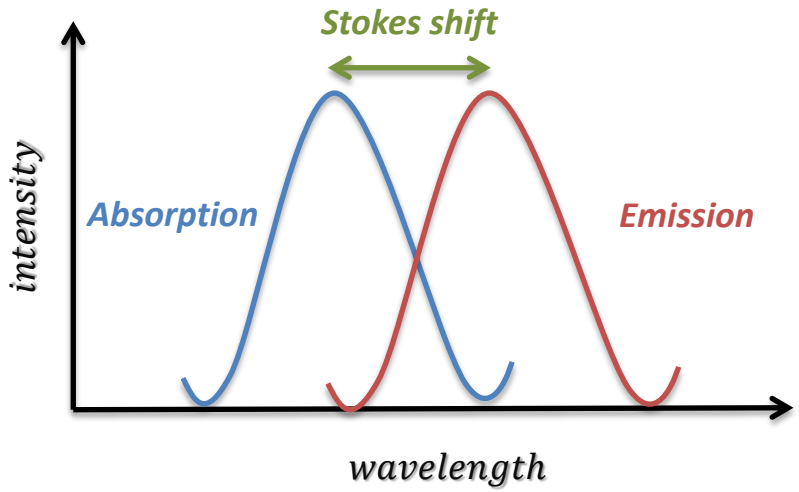

Figure 2.4.1.3: The Stokes shift is responsible for the energy difference between the absorbed and the emitted photons during fluorescence.

2.4.2 Fluorescent labels

The regions of interest within samples are usually labeled with fluorescent markers. Green fluorescent protein (GFP) is a naturally fluorescent protein from the jellyfish *Aequorea victoria* that is widely used to tag points of interest [28]. GFP emits a photon in the green region of the light spectrum when excited by the absorption of light. Biological specimens can be genetically modified to express GFP at specific sites. Additionally, a fluorogen is ligand (fluoregenic ligand); and when it is bound by a protein or RNA structure becomes fluorescent [29]. On the other, autofluorescence is the natural emission of light by biological structures such as mitochondria and lysosomes when they have absorbed light, and is used to distinguish the light originating from artificially added fluorescent markers (fluorophores) [30]. Elastin contains several fluorophores, one of which is a crosslinking tricarboxylic amino acid with a pyridinium ring. This is a similar fluorophore to that found in collagen. Moreover, the autofluorescence (AF) of human skin can be used to measure the level of advanced glycation end-products (AGEs), which are present in higher quantities during several human diseases [31].

Figure 2.4.2.1: Jellyfish Aequorea victoria (on the left) & Bioluminescent plankton in Maldives [32].

3. Materials and methods

3.1 Experimental setup

The OR-PAM modality of the hybrid imaging system (*Figure 3.1.1*) employed a Q-switched Nd:YAG nanosecond laser source (QIR-1064-200-S, CrystaLaser LC, Reno, NV, USA; wave-length: 1,064 nm, pulse energy: 29.4 μJ, pulse duration: ~10 ns, selected repetition rate: 5 kHz, M^2 value: 1.2), which is used for the efficient excitation of the photoacoustic signals. The laser is externally triggered by an arbitrary waveform generator (33612A, Keysight Technologies, Santa Rosa, CA, USA) in synchronisation with data acquisition (DAQ). The beam is tightly focused by a lens on a Lithium Triborate (LBO) second harmonic generation crystal to get a visible wavelength at 532 nm. Following the LBO crystal, a second lens is employed in a telescopic configuration with the focusing one, collimating and expanding the beam by approximately two times.

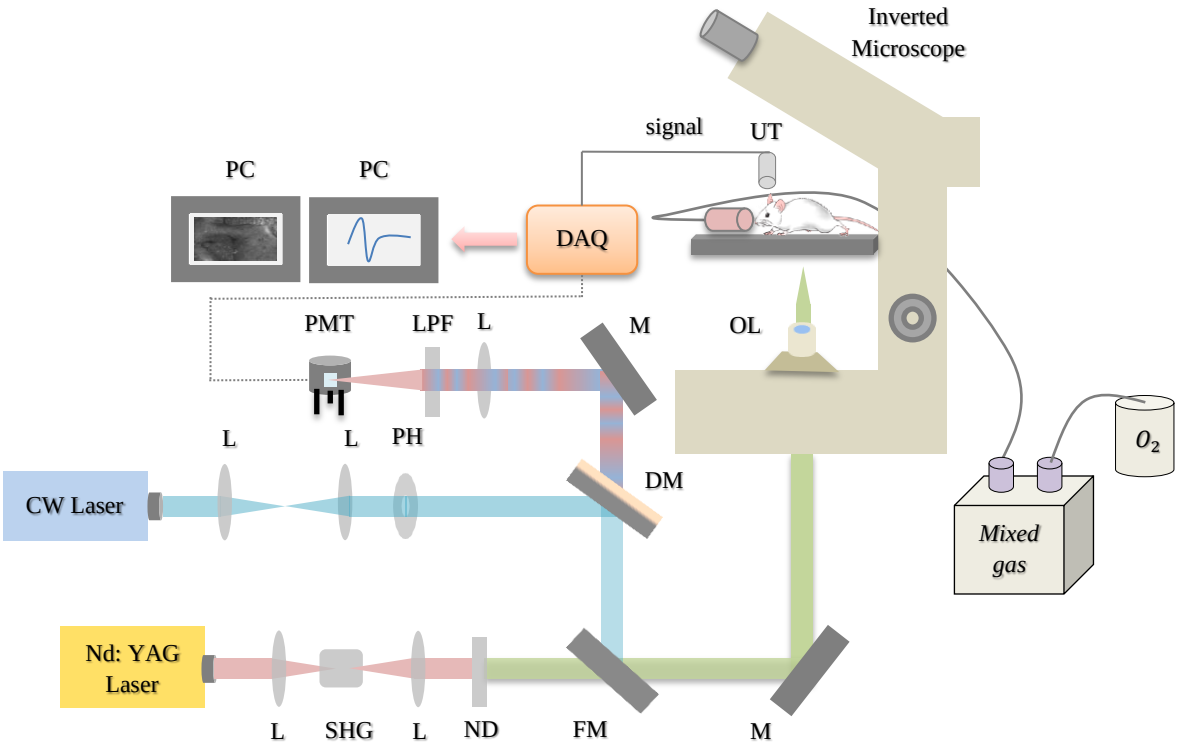

Figure 3.1.1: Scheme of the hybrid imaging system.
L, lens; SHG, second harmonic generation crystal; ND, neutral density filter; FM, flipped mirror; M, mirror; DM, dichroic mirror; PH pinhole; LPF, long-pass filter; PMT, photomultiplier; OL, objective lens; UT, ultrasonic transducer; DAQ, data acquisition card;

A bandpass filter (FF01-531/40-25, Semrock, Rochester, NY, USA) permitting the wavelength transmission from 511 to 551 nm, is subsequently placed to cut off the residual fundamental light, and finally the beam was guided into a properly modified inverted optical microscope.

The laser irradiation is further attenuated through a proper combination of neutral density filters in order to control the total energy deposition at the focal plane. A low numerical aperture (NA_0) objective lens (Achromat 8X, LOMO, St. Petersburg, Russia; air immersion, NA_0: 0.2) is employed for the focusing of the beam onto the specimen. As a sample we used a laboratory-bred mouse (BALB/c). The under investigation area is the right mouse's ear and the aim is to image the ear's vessels together with the autofluorescence (AF) background of the skin. Additionally, as these are in-vivo measurements, the mouse is firstly anaesthetized and subsequently is lied down at the bottom of a custom-made platform, further attached on a set of sub-μm precision XY motorized stages (8MTF-75LS05, Standa, Vilinius, Lithuania) performing a lateral raster scanning in respect to the beam focus. The vertical position of platform is selected manually using the Z-adjustment microscope controls.

In *Figure 3.2* illustrates a top view of the platform. At the center of the platform there is a window with a transparent glass ($75 \times 25\ mm^2$) in order the laser beam to pass through. The ear is fixed by a custom-made "ear-holder" that is wrapped with parafilm. The region between the ear and the holder is filled with a compatible ultrasonic gel layer so that the acoustic waves are not attenuated.

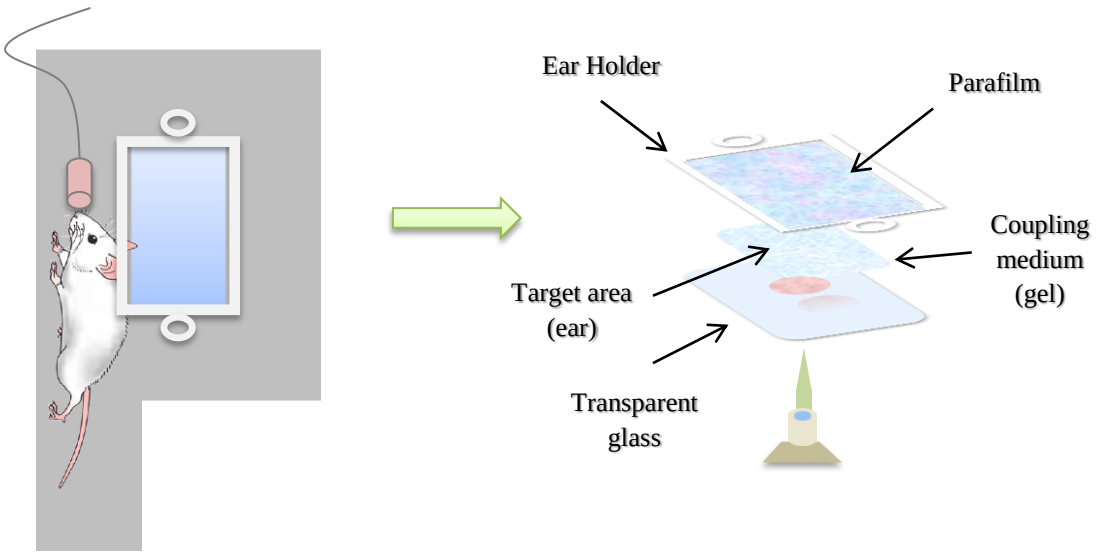

Figure 3.1.2: Scheme of the mouse's platform.
Top view of the platform (on the left) & Zoom-in of the under investigation region (on the right).

The ear-holder is filled with distilled water in order to provide an efficient acoustic coupling between the photoacoustic sources and the detection unit. A spherically focused piezoelectric ultrasonic transducer (~70 MHz central frequency), as immersed into the holder in a confocal and coaxial configuration with respect to the focal volume of the beam, achieving in this manner, the maximum detection sensitivity at the excited region (*Figure 3.1.3*). The detected broadband signals ate additionally amplified using a low noise RF amplifier (AU-1291, Miteq, NY, USA; gain 63 dB) connected to a computer. The detected signal is transmitted to a high gain radio frequency amplifier (AU-1291, Miteq, NY, USA; gain: 63 dB) and digitised by a 14-bit data acquisition card (PCIe-9852, ADLINK, Taipei, Taiwan; sampling rate: 200 MS/s; bandwidth: 90 MHz). To generate a three-dimensional reconstruction, the envelopes of the signals are calculated using the modulus of the Hilbert Transform. Finally, device synchronisation and control of the photoacoustic imaging system are implemented in MATLAB programming environment, whereas respective data processing is performed using custom-made MATLAB scripts, ImageJ.

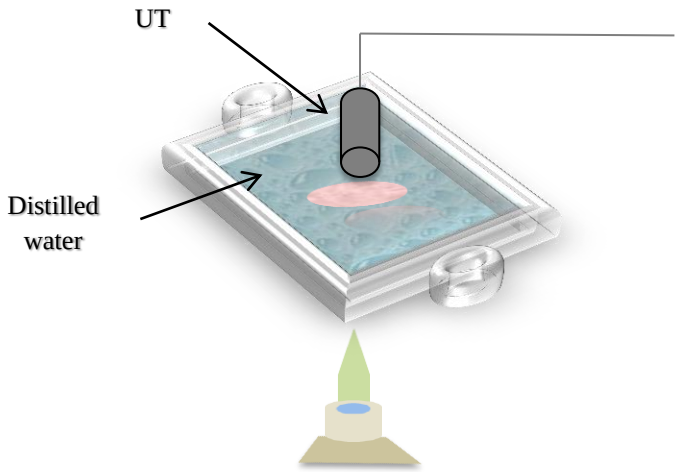

Figure 3.1.3: Acoustic coupling between the photoacoustic signals and the ultrasonic transducer.

Concerning the optical modality of the developed setup (*Figure 3.1.1*), the AF imaging path employs a compact CW diode-pumped laser module (CPS450, Thorlabs, Newton, New Jersey; output power 4.5 mW) emitting at 450 nm, as an excitation source. The beam is initially attenuated through a set of neutral density filters and subsequently guided onto a suitable dichroic mirror (DMLP505, Thorlabs,

Newton, NJ, USA) to be reflected towards the microscope's objective lens which focused the incident light into the sample. A flip mount mirror is used to switch between the photoacoustic (PA) and the autofluorescence (AF) modality, permitting the transmission either of the ns or the CW laser respectively. The sample is similarly raster scanned via the XY motorized stages of the system and the generated autofluorescence signals (AF) are collected in the reflection mode by the objective lens. A long-pass filter (LP03-532RU-25, Semrock Inc., Rochester, New York; edge wavelength: 532 nm) is placed behind the pinhole (PH) to cut off the reflected excitation radiation and isolate exclusively the in-focus emitted AF, which is finally detected by a photomultiplier (PMT) tube (H6780-20, Hamamatsu, Hamamatsu City, Japan). The generated signals are recorded by a high-speed data acquisition (DAQ) card (PCIe-9852, ADLINK, Taipei, Taiwan; sampling rate: 200 MS⁄s; bandwidth: 90 MHz). The control and synchronization of the hybrid setup, as well as the respective data processing and image reconstructions were performed using custom designed software and ImageJ.

3.2 Sample preparation

The aim of our study was to get high resolution images of the ear vasculature and skin of BALB/c mice, bycombining two techniques: OR-PAM and CFM. In order to remove body hair in the under investigation region, we used a depilatory cream ("Veet") for ear hair removal.

In *Figure 3.2.1* we illustrate the preparation process step by step. Firstly, we took the mouse from its cage and put it in an anaesthesia chamber. An apparatus creates a gas mixture of anaesthetic liquid ("IsoFlo" 100% w/w Inhalation Vapour, liquid) and oxygen. The mixed gas is leaded to the anaesthesia chamber so that the mouse is anaesthetized in about 2 minutes due to gas inhalation (step 1). Both the quantity of the anaesthetic liquid and the oxygen are manually adjustable. When we are sure that the mouse loses its senses and doesn't react to a jog, we fix it on an aluminum rectangular area which essentially is the "hair removal area" (step 2). In this step we tried to remove the hair of the mouse's ear. We coated the ear with a depilatory cream ("Veet") for every use and after a few seconds we removed the hair with a cotton swab. It's very important to remove the cream immediately after the coating otherwise a burn can be caused in the ear. Moreover, in order to clean the ear totally

from the cream we washed the coated area out with a wet cotton swab by distilled water. At the whole duration of the procedure, the mouse inhales the mixed gas with the aid of a tube which is fixed on the hair removal area.

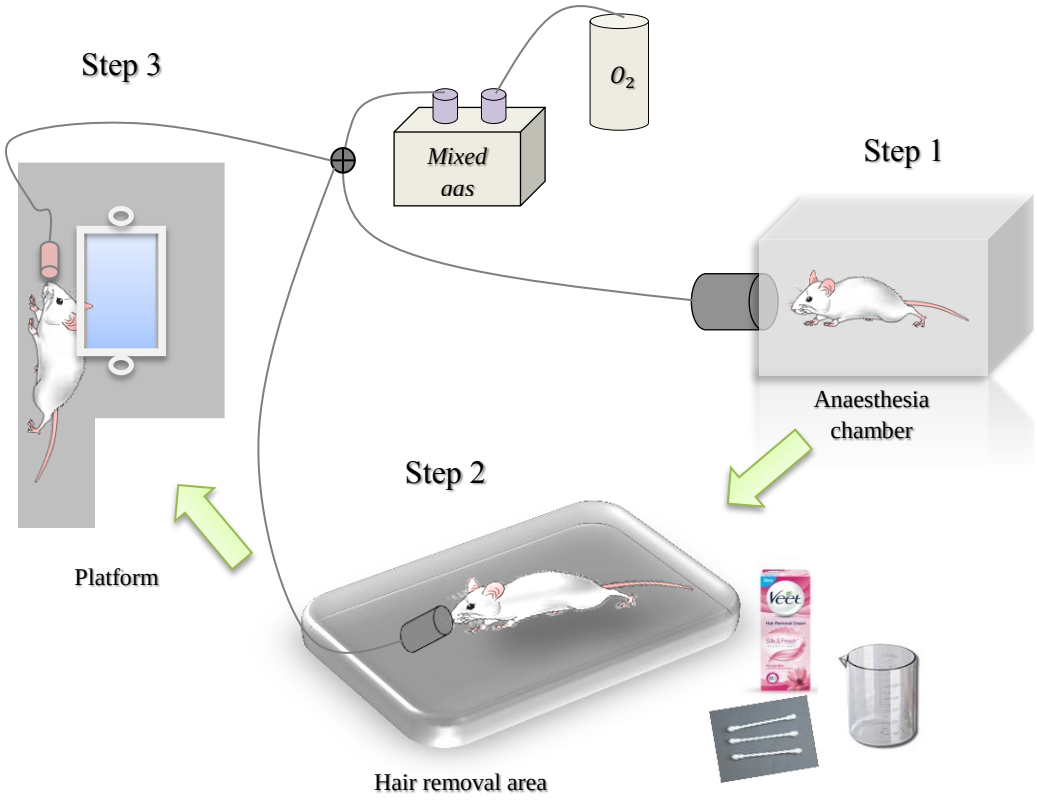

Figure 3.2.1: Preparation process of the sample.

When we finished with step 2, we were ready to fix the sample on the platform and begin the experiment. Again, during the in-vivo experiment, the mouse inhales the anaesthetic gas. The maximum time in which the mouse's life is not at risk is about 1.5-2 hours.

However, it was impossible to entirely remove the hair of the ear because we only reacted on the skin and we couldn't eliminate the pores of the hair. Thus, we expected that we will have some artifacts in our images which however can be reduced by using ImageJ, Java-based image processing software, it has to be mentioned that the pores didn't have negative influence in our study.

3.3 Experimental process

In the previous section the analysis of the preparation process was stopped in step 3, in which the mouse had been fixed onto the platform and experiment could be started. After this step, we tried to find the focus on a specific vessel of the ear using the brightfield mode of the microscope. In order to achieve the vertical positioning of the specimen, we have used the built in microscope's Z-adjustment controls.

Following the procedure, we released the laser beam of the nanosecond laser so that the target area is illuminated. Subsequently, we immersed the ultrasound transducer (UT) into the "ear holder" that was filled with distilled water (*Figure 3.1.3*). The optical focus has to coincide with acoustic focus to achieve the maximunm detection sensitivity, therefore a transducer's alignment procedure was necessary prior any measurement. Then, with the aid of a custom-made software, we set a starting lateral position of the stage and raster-scan of a predefined region took place. Consequently, a 2D picture was formed in our pc-program using resolutions varying from 200x200 to 400x400 pixels respectively.

For the fluorescence technique now, we flipped mirror up, so that the path for CW laser was activated (*Figure 3.1.1*). Again, the laser focus was adjusted manually by a trial and error process and the image was formed using a PMT detector and similar software as were used during OR-PAM technique (details in section 3.1).

3.4 Photographs of the optoacoustic microscopy system

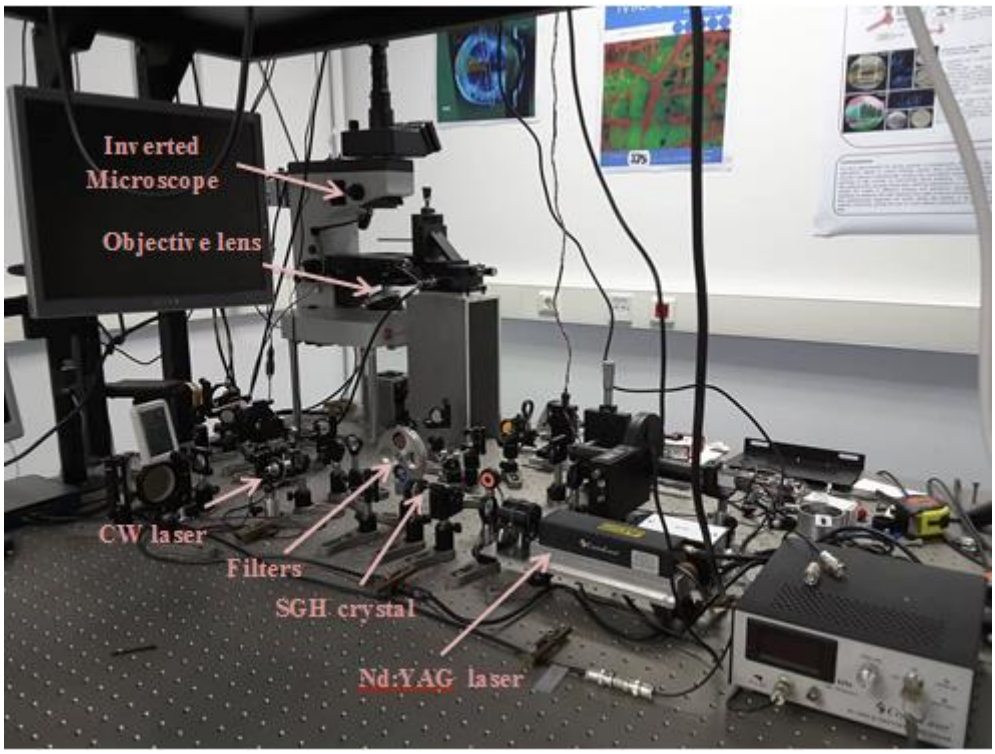

Figure 3.4.1: Setup of the hybrid imaging system

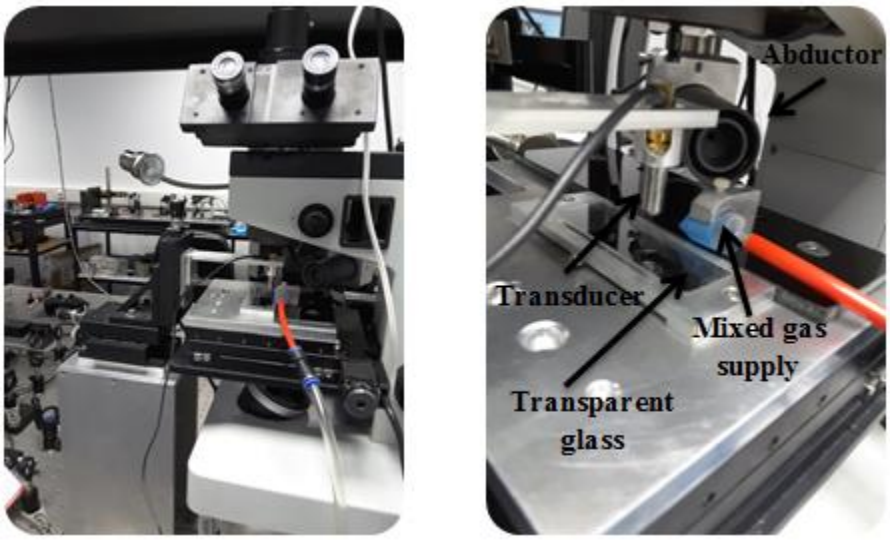

Figure 3.4.2: Scheme of the custom-made platform.

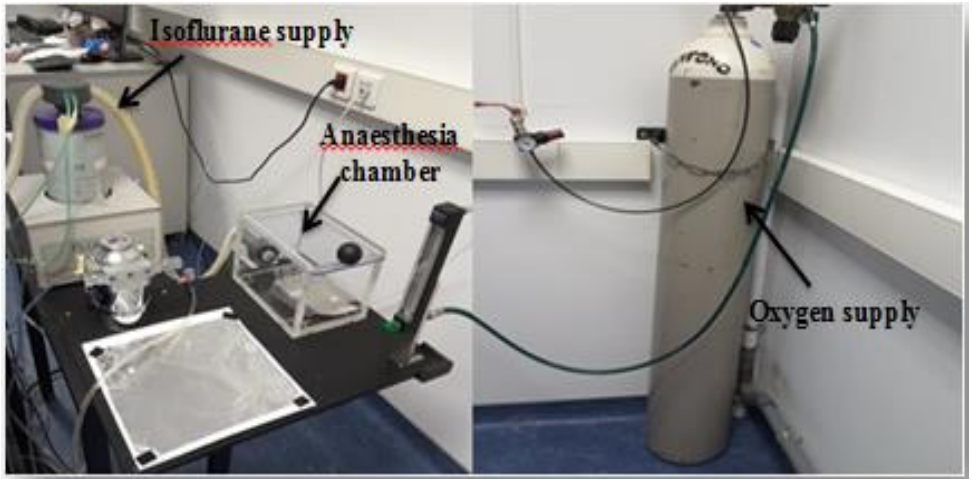

Figure 3.4.3: Anaesthesia configuration.

Figure 3.4.4: Balb/c mouse.

Figure 3.4.5: Balb/c mouse.

4. Results

4.1 Ex-vivo measurements

The first aim of this project was to image the vasculature of the ear of a mouse (BALB/c, black) ex-vivo. The experiment was held initially on ear samples in order to optimize the imaging platform for the subsequent in-vivo measurements. We initially set all the necessary parameters in our setup and aligned the system, before proceeding to the selection of the scanning region, the number of averaging waveforms per scanning point and finally the resolution of the image. These settings also determined the duration of the raster-scan which is essentially the time required to form the image. Representative images of such measurements are illustrated bellow:

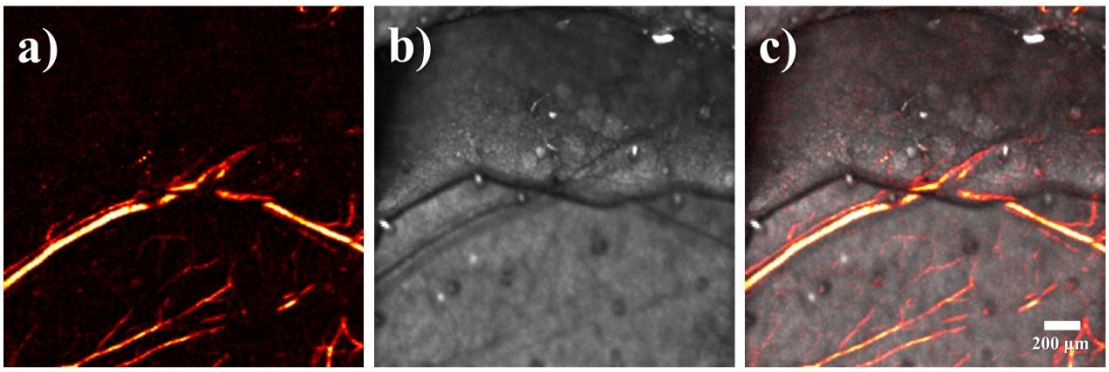

Figure 4.1.1: Vasculature of the ear of a BALB/C black mouse (ex-vivo).
a) Maximum amplitude projection OR-PAM, b) CFM image, c) Composite image (scanned region: $2000 \times 2000\ \mu m^2$*, resolution:* 300×300 *pixels, averages: 25)*

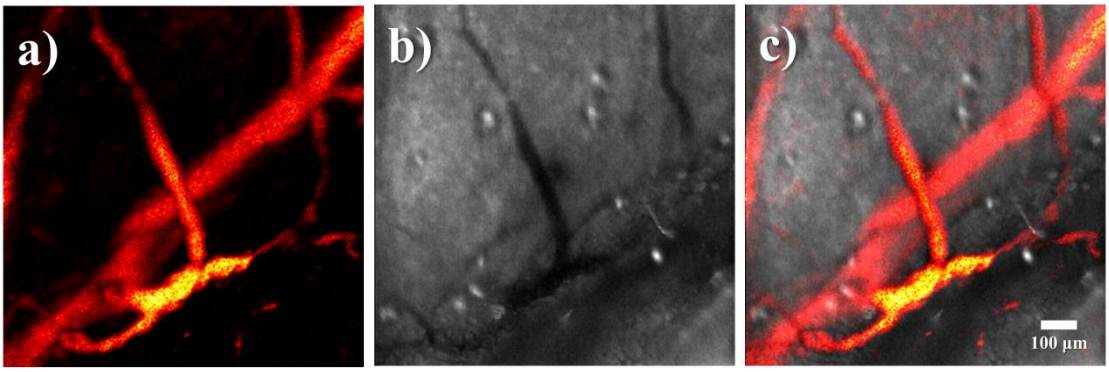

Figure 4.1.2: Vasculature system of the ear of a BALB/C black mouse (ex-vivo).
a) Maximum amplitude projection OR-PAM image, b) CFM image c) Composite image (scanned region: $1000 \times 1000\ \mu m^2$*, resolution:* 400×400 *pixels, averages: 20)*

In the figures above, we can clearly delineate the capillary vessels of the ear with high resolution and contrast. The first images correspond to the OR-PAM technique and ware formed by recording the maximum amplitude projection of the generated photoacoustic signals, as a result of the strong absorption of visible radiation by hemoglobin. The second image was formed with the aid of the CFM technique, which records the intrinsic autofluorescence of several tissue components such as elastin, collage and melanin.

Each figure illustrates a particular region from the same sample. In order to get representative images of the vasculature, we scanned a number of samples at several regions. Additionally, it is noticeable that the images corresponding to the fluorescence technique present limited hair follicles. This is due to the fact that the specific sample didn't have a big amount of hairs, and as a result we managed to wipe them out completely. In *Figure 4.1.3*, we represent two more set of images:

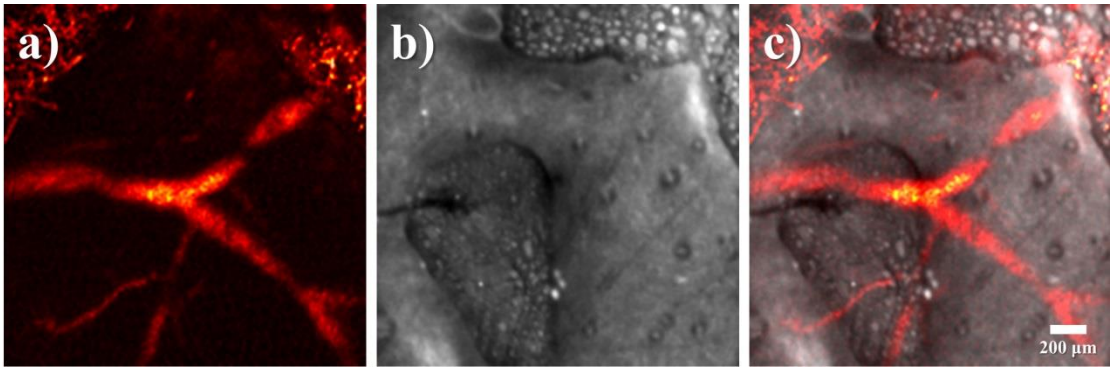

Figure 4.1.3: Vasculature of the ear of a BALB/C black mouse (ex-vivo).
a) Maximum amplitude projection OR-PAM, b) CFM image, c) Composite image (scanned region: $2000 \times 2000\ \mu m^2$*, resolution:* 200×200 *pixels, averages: 30)*

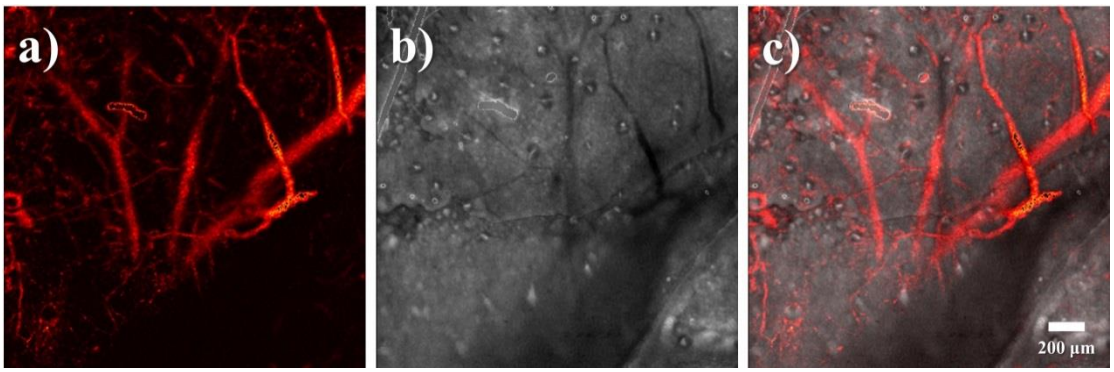

Figure 4.1.4: Vasculature of the ear of a BALB/C black mouse (ex-vivo).
a) Maximum amplitude projection OR-PAM, b) CFM image, c) Composite image (scanned region: $2000 \times 2000\ \mu m^2$*, resolution:* 400×400 *pixels, averages: 20)*

All images were reconstructed through the modulus of Hilbert Transformation using Matlab software. Furthermore, the images were processed by the Java-based image processing program, ImageJ. In the following two figures, we can notice some blurred "pores" at the fluorescence's images. In this case, the sample was again a BALB/c mouse, however of a white fur. This strain of mouse has a big amount of hair on its ear, and this is the reason why some hair follicles remained after the depilation. For the sake of a nice image we tried to attenuate the fluorescence signal arising from the hair follicles using ImageJ.

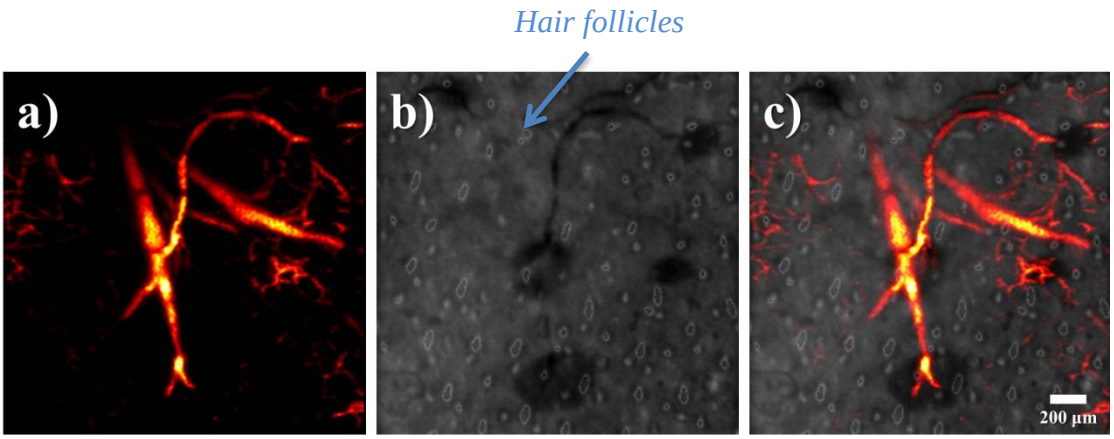

Figure 4.1.5: Vasculature of the ear of a BALB/C black mouse (ex-vivo).
a) Maximum amplitude projection OR-PAM, b) CFM image, c) Composite image (scanned region: $2000 \times 2000\ \mu m^2$*, resolution:* 300×300 *pixels, averages: 25)*

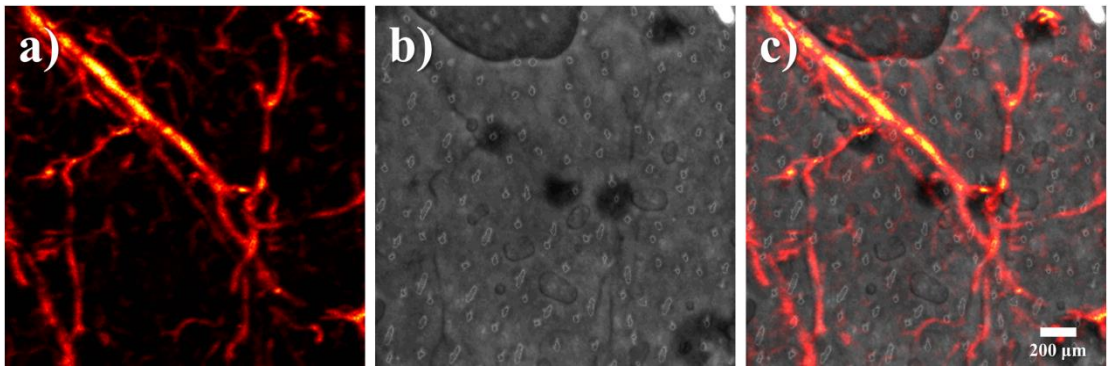

Figure 4.1.6: Vasculature of the ear of a BALB/C black mouse (ex-vivo).
a) Maximum amplitude projection OR-PAM, b) CFM image, c) Composite image (scanned region: $2000 \times 2000\ \mu m^2$*, resolution:* 400×400 *pixels, averages: 20)*

In *Figure 4.1.7* we are demonstrating a maximum amplitude projection image that was generated through the OR-PAM technique in an additional sample. This image results from the digital stitching of two adjacent regions of the same sample which was the result of the processing of two different images. Moreover, the processing of the image was done by using Fiji Java-based image processing software. Specifically, we chose the command "stitching" at plugins of the program.

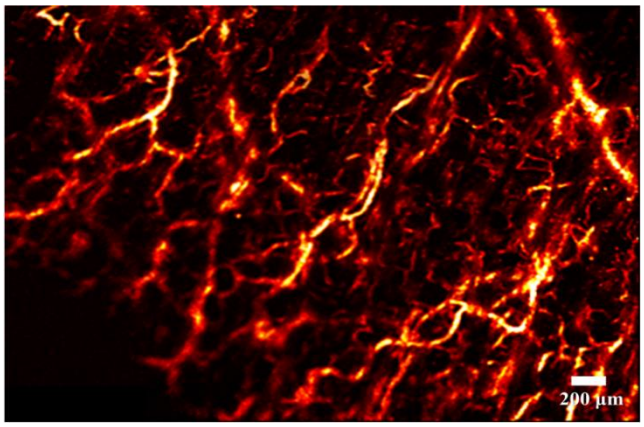

Figure 4.1.7: Vasculature of the ear of a BALB/C black mouse (ex-vivo). *Maximum amplitude projection OR-PAM- Merging of two adjacent regions of the vasculature (Details of two images: scanned region:* $2000 \times 2000\ \mu m^2$*, resolution:* 300×300 *pixels, averages: 25 – Final image's size:* 387×303 *pixels).*

4.2 In-vivo measurements

Regarding the previous section we mentioned that the ex-vivo experiments were aimed to lead us to the development of an imaging platform for in-vivo observations in mouse models and to the modification of our set-up. Herewith, we are representing our data of in-vivo measurements. Finally, we managed to take in-vivo data which was the final ain of the current thesis. The mouse was anaesthetized during the experiments and after that it took five minutes to wake up. The second measurement (*Figure 4.2.1*) took place two weeks after the first. In the figures bellow we are showing the recorded images:

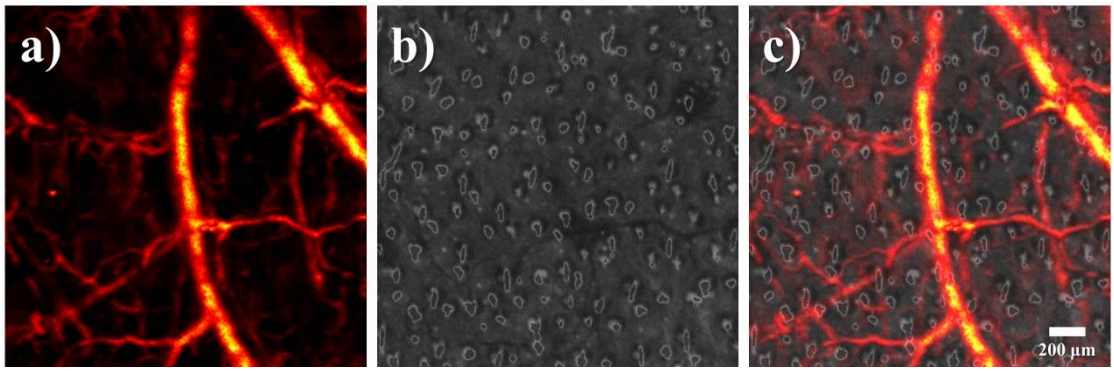

Figure 4.2.1: Vasculature system of the ear of a BALB/C white mouse (in-vivo).
a) Maximum amplitude projection OR-PAM, b) CFM image, c) Composite image (scanned region: $2000 \times 2000\ \mu m^2$*, resolution:* 400×400 *pixels, averages: 20).*

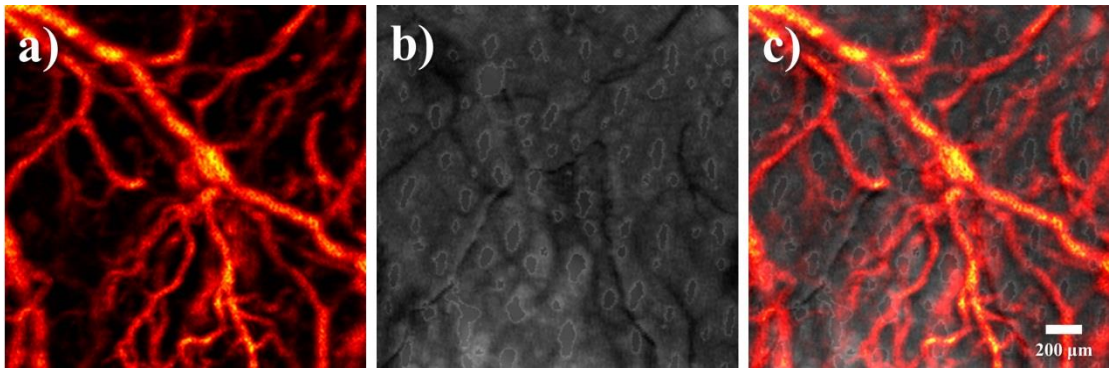

Figure 4.2.2: Vasculature system of the ear of a BALB/C white mouse (in-vivo).
*a) Maximum amplitude projection OR-PAM, b) CFM image, c) Composite image (scanned region: 1*$500 \times 1500\ \mu m^2$*, resolution:* 300×300 *pixels, averages: 25).*

5. Conclusions

To sum up, in our study we integrated optical resolution photoacoustic microscopy (OR-PAM) and confocal fluorescence microscopy (CFM). We employed label-free imaging by taking advantage of endogenous absorbers such as hemoglobin, melanin, elastin and collagen providing complementary contrasts. Consequently, we managed to illustrate in-vivo the vasculature system of a mouse's ear. Furthermore, our data, can reveal some quantitative information as regards to the ear's vasculature. We can observe that larger vessels have a diameter about 100-150 μm and the capillaries have a diameter about 25-80 μm. Also, we can obtain information about the existence of endogenous contrast agents whose determination can be based on the excitation wavelength and the respective spectral detection as regards to the fluorescence microscopy technique. Moreover, this hybrid approach could be used for the study of several pathological condition such as melanoma, tumors, or carcinogenesis.

Generally, the photoacoustic microscopy has the following notable features: 1) breaks through the optical diffusion limit, with highly scalable spatial resolution and maximum imaging depth in both optical and acoustic domains, 2) images optical absorption contrast with good sensitivity without speckle artifacts, 3) can essentially image all molecules at their absorbing wavelength, 4) is capable of functional and metabolic imaging using endogenous contrast agents. Therefore, there is a direction for more future PAM developments particularly in vascular biology, dermatology, oncology, cardiology and general clinical human studies.

According to our study, the future plans target on a biological application which will have as main concept "the study of the development of glioblastoma tumors in brain". We aim to subcutaneously inject a spheroid of cancerous cells in mouse models in-vivo in order to achieve their detection using our hybrid imaging modality as a powerful tool for pre-clinical applications.

References

1. B. Amos, Nature Cell Biology, E151-E152 (2000).
2. Ntziachristos, V. Going deeper that microscopy: The optical imaging frontier in biology. Nat. Methods 7, 603-614 (2010).
3. Wang LHV, Hu S. Photoacoustic tomography: in vivo imaging from organelles to organs. Science 2012;335(6075):1458–62.
4. https://en.wikipedia.org/wiki/Photophone.
5. Wang LV, Wu H-I, Biomedical optics: principles and imaging, Hoboken NJ: Wiley-Interscience; 2007 xiv, 362.
6. https://en.wikipedia.org/wiki/Photoacoustic_effect.
7. Paul Beard, Biomedical photoacoustic imaging, Interface Focus, 602–631, doi:10.1098/rsfs.2011.0028, (2011).
8. Yong Zhou, Junjie Yao, and Lihong V. Wang: Tutorial on photoacoustic tomography J Biomed Opt. 2016 Jun; 21(6): 061007. Published online 2016 Apr 18. doi: 10.1117/1.JBO.21.6.061007.
9. H.F. Zhang; K. Maslov; G. Stoica; L.V. Wang (2006). "Functional photoacoustic microscopy for high-resolution and noninvasive in vivo imaging". Nature Biotechnology. 24: 848–851. doi:10.1038/nbt1220.
10. K. Maslov, G. Stoica, and L. H. V. Wang, Optics Letters **30**(6), 625–627 (2005).
11. Bin Rao, Li Li, Konstantin Maslov, and Lihong Wang, "Hybrid-scanning optical-resolution photoacoustic microscopy for in vivo vasculature imaging", Opt Lett. 2010 May 15; 35(10): 1521–1523, PMID: 20479795, May. 2010.
12. George J. Tserevelakis, Stella Avtzi, Miltiadis K. Tsilimbaris, Giannis Zacharakis, "Delineating the anatomy of the ciliary body using hybrid optical and photoacoustic imaging," J. Biomed. Opt. 22(6), 060501 (2017), doi: 10.1117/1.JBO.22.6.060501.
13. Bin Rao, Li Li, Konstantin Maslov, and Lihong Wang, "Hybrid-scanning optical-resolution photoacoustic microscopy for in vivo vasculature imaging", Opt Lett. 2010 May 15; 35(10): 1521–1523, PMID: 20479795, May. 2010, page 4.
14. J. Yao and L.V. Wang: Photoacoustic microscopy: A review by wiley (2012), page 2.
15. https://en.wikipedia.org/wiki/Numerical_aperture.
16. Cargille, John J. (1985). "Immersion oil and the microscope" (2nd ed.).
17. H. Azhari, Basics of biomedical ultrasound for engineers 2010, Wiley : IEEE: Hoboken, N.J.
18. J. Yao and L.V. Wang: Photoacoustic microscopy: A review by wiley (2012), page 4.
19. S. Hu, K. Maslov, and L. V. Wang, Optics Letters **36**(7), 1134–1136 (2011).
20. Winkler AM, Maslov K, Wang LV. Noise-equivalent sensitivity of photoacoustics. J Biomed Opt 2013;18(9):097003.
21. J. Yao and L.V. Wang: Photoacoustic microscopy: A review by wiley (2012), page 7.
22. D. Zink, A. H. Fischer, and J.A.Nickerson, NatureReviews Cancer **4**(9), 677–687 (2004).
23. Wasserman DH (January 2009). "Four grams of glucose". American Journal of Physiology Endocrinology and Metabolism. 296 (1): E11-21. doi:10.1152/ajpendo.90563.2008.
24. J. Yao and L.V. Wang: Photoacoustic microscopy: A review by wiley (2012), page 8.
25. Single-molecule fluorescence microscopy review: shedding new light on old problems, Sviatlana Shashkova and Mark C. Leake, Published online 2017 Jul 21. Prepublished online 2017 Jul 10. doi: 10.1042/BSR20170031.

26. H. H. Jaffe and Albert L. Miller "The fates of electronic excitation energy" J. Chem. Educ., 1966, 43 (9), p 469 DOI**:**10.1021/ed043p469.
27. E. B. Priestley and A. Haug "Phosphorescence Spectrum of Pure Crystalline Naphthalene" J. Chem. Phys. 49, 622 (1968), DOI:10.1063/1.1670118.
28. Cox, Michael; Nelson, David R.; Lehninger, Albert L (2008). Lehninger principles of biochemistry. San Francisco: W.H. Freeman. ISBN 0-7167-7108-X.
29. Szent-Gyorgyi C, Schmidt BF, Creeger Y, et al. (April 2008). "Fluorogen-activating single-chain antibodies for imaging cell surface proteins". Nature Biotechnology (Abstract). **26** (2): 235–40. doi:10.1038/nbt1368. PMID 18157118. We report here the development of protein reporters that generate fluorescence from otherwise dark molecules (fluorogens).
30. Monici M. (2005). "Cell and tissue autofluorescence research and diagnostic applications". Biotechnol Annu. Rev. 11: 227–56. doi:10.1016/S1387-2656(05)11007-2. PMID 16216779.
31. Gerrits EG, Smit AJ, Bilo HJ (March 2009). "AGEs, autofluorescence and renal function". Nephrol. Dial. Transplant. 24 (3): 710–3. doi:10.1093/ndt/gfn634. PMID 19033250.
32. http://blog.microbiologics.com/green-fluorescent-proteins-shining-new-light-on-food-qc/.